# PRIN/SPRIN: On Extracting Point-wise Rotation Invariant Features

Yang You, Yujing Lou, Ruoxi Shi, Qi Liu, Yu-Wing Tai, Lizhuang Ma, Weiming Wang, Cewu Lu *Member, IEEE* 

Abstract—Point cloud analysis without pose priors is very challenging in real applications, as the orientations of point clouds are often unknown. In this paper, we propose a brand new point-set learning framework PRIN, namely, Point-wise Rotation Invariant Network, focusing on rotation invariant feature extraction in point clouds analysis. We construct spherical signals by Density Aware Adaptive Sampling to deal with distorted point distributions in spherical space. Spherical Voxel Convolution and Point Re-sampling are proposed to extract rotation invariant features for each point. In addition, we extend PRIN to a sparse version called SPRIN, which directly operates on sparse point clouds. Both PRIN and SPRIN can be applied to tasks ranging from object classification, part segmentation, to 3D feature matching and label alignment. Results show that, on the dataset with randomly rotated point clouds, SPRIN demonstrates better performance than state-of-the-art methods without any data augmentation. We also provide thorough theoretical proof and analysis for point-wise rotation invariance achieved by our methods. Our code is available on https://github.com/qq456cvb/SPRIN.

Index Terms—Point cloud, object analysis, rotation invariance, feature learning

#### 1 Introduction

Deep learning on point clouds has received tremendous interest in recent years. Since depth cameras capture point clouds directly, efficient and robust point processing methods like classification, segmentation and reconstruction have become key components in real-world applications. Robots, autonomous cars, 3D face recognition and many other fields rely on learning and analysis of point clouds.

Existing works like PointNet [1] and PointNet++ [2] have achieved remarkable results in point cloud learning and shape analysis. But they focus on objects with canonical orientations. In real applications, these methods fail to be applied to rotated shape analysis since the model orientation is often unknown as a priori, as shown in Figure 1. In addition, existing frameworks require massive data augmentation to handle rotations, which induces unacceptable computational cost.

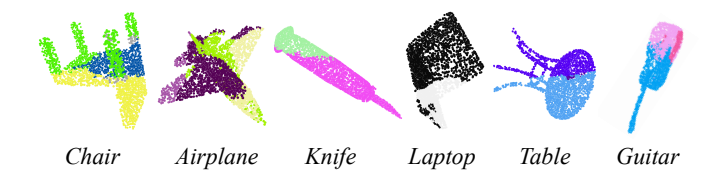


Fig. 1. **PointNet++ part segmentation results on rotated shapes.** When trained on objects with canonical orientations and evaluated on rotated ones, PointNet++ is unaware of their orientations and fails to segment their parts out.

Spherical CNN [3] and a similar method [4] try to solve this

- Yang You, Yujing Lou, Ruoxi Shi, Qi Liu, Lizhuang Ma, Weiming Wang, Cewu Lu are with Shanghai Jiao Tong University, Shanghai, 200240, China. Yu-Wing Tai is with the Department of Computer Science and Engineering, The Hong Kong University of Science and Technology, Hong Kong.
- Weiming Wang is the corresponding author. E-mail: wangweiming@sjtu.edu.cn

problem and propose a global feature extracted from continuous meshes, while they are not suitable for point clouds since they project 3D meshes onto their enclosing spheres using a ray casting scheme. Difficulty lies in how to apply spherical convolution in continuous domain to sparse point clouds. Besides, by projecting onto unit sphere, their method is limited to processing convex shapes, ignoring any concave structures. Therefore, we propose a point-wise rotation invariant network (PRIN) to handle these problems. Firstly, we observe the discrepancy between unit spherical space and Euclidean space, and propose Density Aware Adaptive Sampling (DAAS) to avoid biases. Secondly, we come up with Spherical Voxel Convolution (SVC) without loss of rotation invariance, which is able to capture any concave information. Furthermore, we propose Point Re-sampling module that helps to extract rotation invariant features for each point.

PRIN is a network that directly takes point clouds with random rotations as the input, and predicts both categories and pointwise segmentation labels without data augmentation. It absorbs the advantages of both Spherical CNN and PointNet-like network by keeping rotation invariant features, while maintaining a one-to-one point correspondence between the input and output. PRIN learns rotation invariant features at spherical voxel grids. Afterwards, these features could be aggregated into a global descriptor or perpoint descriptor to conduct model classification or part segmentation, respectively. We rigorously prove the point-wise rotation invariance of PRIN under certain conditions.

In addition, we extend our PRIN framework and propose a sparse version of PRIN called SPRIN. SPRIN considers input as the Dirac delta function and gives rotation invariant features when the filter is constant on the left coset of z-axes rotation.

We experimentally compare PRIN and SPRIN with various state-of-the-art approaches on the benchmark dataset: ShapeNet part dataset [5] and ModelNet40 [6]. Additionally, both PRIN and SPRIN can be applied to 3D point matching and label alignment. Both PRIN and SPRIN exhibit remarkable performance. SPRIN also achieves the state-of-the-art performance on part segmenta-

tion.

The key contributions of this paper are as follows:

- We design two novel deep network processing pipelines PRIN/SPRIN that extracts rotation invariant point-level features
- Three key modules: Density Aware Adaptive Sampling (DAAS), Spherical Voxel Convolution (SVC) and Point Re-sampling are proposed for PRIN.
- Rigorous proof of point-wise rotation invariance is given for both PRIN and SPRIN frameworks.
- We show that PRIN/SPRIN can be used for point cloud part segmentation, classification, 3D point matching and label alignment under different rotations. SPRIN achieves the state-of-the-art performance on part segmentation.

A preliminary version of this work was presented in AAAI2020 [7]. In this study, we extend it in two fundamental aspects. First, we provide thorough theoretical analysis and proof for the point-wise rotation invariance in PRIN, and some necessary filter conditions are proposed. With this revised version of spherical voxel convolution, we achieve much better results than our previous work. Second, we extend PRIN to sparse domain, where the Dirac delta function is leveraged and sparse correlation is proposed with guaranteed rotation invariance. The sparse version of PRIN, which is named SPRIN, achieves the state-of-the-art performance on ShapeNet part segmentation.

#### 2 RELATED WORK

#### 2.1 Rotation invariant Features

Rotation Invariance is often regarded as a preliminary to the success of template matching and object detection, in both 2D and 3D domains.

The development of rotation invariant features from geometries could be retrospected to manual designed features, including Structural Indexing [8], Signature of Histogram Orientations (SHOT) [9], CGF [10] and Snapshots [11]. They construct a local reference frame (LRF) which aligns the model into its canonical pose in order to extract rotation invariant point features. However, these methods depend on local surface variations, therefore are sensitive to noise and point densities. Besides, these descriptors rely on delicate hand-craft design, and could only capture low-level geometric features. For a more complete review on traditional feature descriptors, we refer to [12].

Recently, some papers consider generalizations of 2D CNNs that exploit larger groups of symmetries [13], [14], including the 2D/3D rotation group [15]. Spherical CNN [3] and a similar method [4] propose to extract global rotation invariant features from continuous meshes, while they are not suitable for point clouds since they project 3D meshes onto their enclosing spheres using a ray casting scheme.

In parallel to group invariant/equivalent convolutions, some researchers incorporate rotation invariant point-level convolutions. SRINet [16] proposes the point projection feature, which is invariant to the rotation of the input point cloud. It introduces an efficient key point descriptor to assign each point with different response and help recognize the overall geometry. Poulenard et al. [17] employ a spherical harmonics based kernel at different layers of a point-based PCNN architecture. Kim et al. [18] take advantages of multi-level abstraction based on graph convolutional neural networks, which constructs a descriptor hierarchy to encode

rotation invariant shape information of an input object in a bottomup manner. Zhang et al. [19] use low-level rotation invariant geometric features such as distances and angles to design a convolution operator for point cloud learning. Li et al. [20] present a network architecture to embed rotation invariant representations into features, encoding local relations between points and their neighbors, and the global shape structure.

# 2.2 Deep Learning on 3D Models

As the consequence of success in deep learning, various methods have been proposed for better understanding 3D models. Convolutional neural networks are applied to volumetric data since its format is similar to pixel and easy to transfer to existing frameworks. 3D ShapeNet [6] and VoxNet [21] are pioneers introducing fully-connected networks to voxels. However, dealing with voxel data requires large memory and its sparsity also makes it challenging to extract particular features from big data.

Another research branch is multi-view methods. MVCNN [22] renders 3D models into multi-view images and propagates these images into traditional convolutional neural networks. These approaches are limited to simple tasks like classification and not suitable for 3D part segmentation, key point matching or other tasks.

Dealing with point clouds directly is another popular branch, among which PointNet [1] is the pioneer in building a general framework for learning point clouds. Since then, many structures are proposed to learn from point clouds. PointNet++ [2] extends PointNet by introducing a hierarchical structure. RSNet [23] is combines a novel slice pooling layer, Recurrent Neural Network (RNN) layers, and a slice unpooling layer, to better propagate features among different parts. SplatNet [24] uses sparse bilateral convolutional layers to enable hierarchical and spatially-aware feature learning. DGCNN [25] proposes EdgeConv, which explicitly constructs a local graph and learns the embeddings for the edges in both Euclidean and semantic spaces. As a followup, LDGCNN [26] links the hierarchical features from different dynamic graphs based on DGCNN. SO-Net [27] models the spatial distribution of point cloud by building a Self-Organizing Map (SOM) and its receptive field can be systematically adjusted by conducting point-to-node k nearest neighbor search. SpiderCNN [28] designs the convolutional filter as a product of a simple step function that captures local geodesic information and a Taylor polynomial that ensures the expressiveness. DeepSets [29] provides a family of functions which are permutation-invariant and gives a competitive result on point clouds. Point2Sequence [30] uses a recurrent neural network (RNN) based encoder-decoder structure, where an attention mechanism is proposed to highlight the importance of different area scales. Kd-Network [31] utilizes kd-tree structures to form the computational graph, which learns from point clouds hierarchically. However, few of them are robust to random rotations, making it hard to apply them to real applications.

# 3 PRELIMINARIES

# 3.1 Unit Sphere: $S^2$

A point s in 2-dimensional sphere can be uniquely described by its azimuthal and polar angles:  $(\alpha, \beta)$ , where  $\alpha \in [0, 2\pi], \beta \in [0, \pi]$ . Furthermore, if we denote  $n = (0, 0, 1)^T$  as the north pole, the coordinate of s is given by  $Z(\alpha)Y(\beta)n$ , where  $Z(\cdot)$  and  $Y(\cdot)$  represent the rotation matrix around z and y axes, respectively.

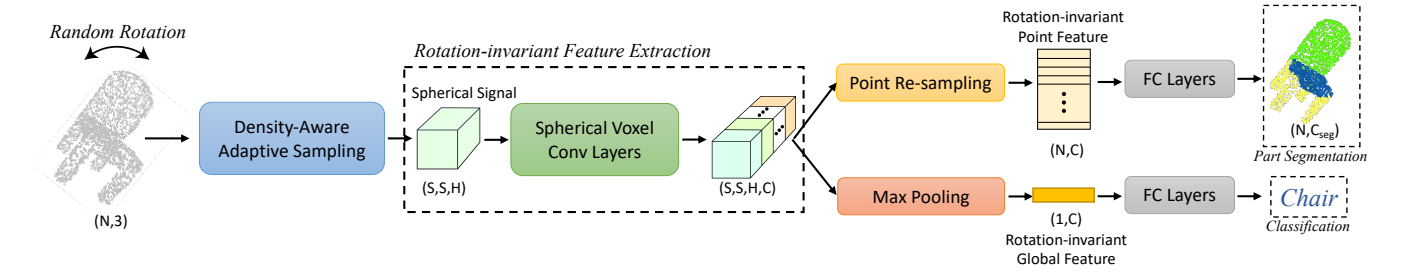


Fig. 2. **PRIN Architecture.** Our network takes sparse points as input, and then uses Density-Aware Adaptive Sampling to transform the signals into spherical voxel grids. This spherical voxel signals is then passed through several Spherical Voxel Convolution layers, ending with a feature at each spherical voxel grid. Any point feature can be extracted by point re-sampling, which is used to do point-wise part segmentation. All these voxel features can also be max-pooled to get a global feature, which is suitable for classification.

# 3.2 Unit Spherical Space: $S^2 \times H$

Any point x in unit ball can be uniquely parameterized by an augmented spherical coordinate:  $(s(\alpha,\beta),h)$ , where  $s(\alpha,\beta) \in S^2$  denotes its location when projected to unit sphere, and  $h \in H = [0,1]$  represents the radial distance to the origin. It is obvious that this parametrization is bijective.

# 3.2.1 Rotation Transformation

Consider an arbitrary rotation transformation Q applied to point  $x \in S^2 \times H$ :

$$Qx(\alpha, \beta, h) = (Qs(\alpha, \beta), h)$$
  
=  $(QZ(\alpha)Y(\beta)n, h).$  (1)

Intuitively, Q rotates the point around the origin, while keeping its radial distance towards the origin.

# 3.3 3D Rotation Group: SO(3)

The 3D rotation group, often denoted SO(3), which is termed "special orthogonal group", is the group of all rotations about the origin of three-dimensional Euclidean space  $\mathbb{R}^3$  under the operation of composition. Almost every element (except for singularities) in SO(3) can be uniquely parameterized by ZYZ-Euler angles:  $(\alpha,\beta,\gamma)$ , where  $\alpha\in[0,2\pi],\beta\in[0,\pi]$ , and  $\gamma\in[0,2\pi]$ . In matrix form, for any element  $R\in SO(3)$ ,  $R(\alpha,\beta,\gamma)=Z(\alpha)Y(\beta)Z(\gamma)$ . This parametrization is also bijective almost everywhere.

#### 3.3.1 Rotation Transformation

Consider an arbitrary rotation transformation Q applied to another rotation  $R \in SO(3)$ , which is a transformation composition:

$$QR(\alpha, \beta, \gamma) = QZ(\alpha)Y(\beta)Z(\gamma). \tag{2}$$

# 4 PRIN: An Exact Point-wise Rotation Invariant Network

#### 4.1 Problem Statement

Given a set of unordered points  $\mathcal{X} = \{x_i\}$  with  $x_i \in \mathbb{R}^{d^{in}}$  and  $i = 1, \dots, N$ , where N denotes the number of input points and  $d^{in}$  denotes the dimension of input features at each point, which can be positions, colors, etc. Our goal is to produce a set of pointwise features  $\mathcal{Y} = \{y_i\}$  with  $y_i \in \mathbb{R}^{d^{out}}$  and  $i = 1, \dots, N$ , which are invariant to input orientations. PRIN can be modeled as a rotation invariant function  $\mathcal{F}: \mathcal{X} \mapsto \mathcal{Y}$ . Although the problem

and the method developed are general, we focus on the case  $d_{in}=3$  using only Euclidean coordinates as the input. To implement function  $\mathcal{F}$ , we design mainly three modules: (1) Density Aware Adaptive Sampling (DAAS) module  $\Gamma:\mathbb{R}^{N\times 3}\to\mathbb{R}^{S^2\times H}$  that constructs spherical signals; (2) Spherical Voxel Convolution (SVC) module  $\Phi:\mathbb{R}^{S^2\times H\times C_{in}}\to\mathbb{R}^{S^2\times H\times C_{out}}$  that extracts rotation invariant features; (3) Point Re-sampling module  $\Lambda:\mathbb{R}^{S^2\times H\times C_{out}}\to\mathbb{R}^{N\times C_{out}}$  that re-samples points from spherical signals. We will explain these modules in the following sections and the whole pipeline is shown in Figure 2.

# 4.2 Density Aware Adaptive Sampling

In this step, the objective is to build spherical signals from irregular point clouds. Nonetheless, if we sample point clouds uniformly into regular spherical voxels, we will meet a problem: points around the pole appear to be more sparse than those around the equator in spherical coordinates, which brings a bias to the resulting spherical voxel signals. To address this problem, we propose Density Aware Adaptive Sampling (DAAS). DAAS leverages a non-uniform filter to adjust the density discrepancy brought by spherical coordinates, thus reducing the bias. This process can be modeled as  $\Gamma:\mathbb{R}^{N\times 3}\to\mathbb{R}^{S^2\times H}$ .

In practice, we divide unit spherical space into spherical voxels, which are indexed by  $(i,j,k) \in I \times J \times K$ , where  $I \times J \times K$  is the spatial resolution, also known as the bandwidth [32]. Each spherical voxel is represented by its center  $(s(a_i,b_j),c_k)$  with  $a_i=\frac{i}{I}\cdot 2\pi,\ b_j=\frac{j}{J}\cdot \pi,$  and  $c_k=\frac{k}{K}$ . The division of unit spherical space is shown in the left of Figure 3.

We first map each point  $x_i \in \mathcal{X}$  from Euclidean space  $\mathbb{R}^3$  to unit spherical space  $S^2 \times H$  by calculating its spherical coordinates  $(s(\alpha_i, \beta_i), h_i)$ , and then calculate the spherical signal  $f: S^2 \times H \to \mathbb{R}$  as follows:

$$f(a_i, b_j, c_k) = \frac{\sum_{n=1}^{N} w_n \cdot (\xi - ||h_n - c_k||)}{\sum_{n=1}^{N} w_n},$$
 (3)

where  $w_n$  is a normalizing factor that is defined as

$$w_n = \mathbf{1}(\|\alpha_n - a_i\| < \xi)$$

$$\cdot \mathbf{1}(\|\beta_n - b_j\| < \eta \xi)$$

$$\cdot \mathbf{1}(\|h_n - c_k\| < \xi),$$
(4)

 $\xi$  is a predefined threshold filter width and  $\eta$  is a density aware factor explained in the next subsection. We use  $(\xi - ||h_n - c_k||)$  in

Equation 3 because it captures information along H axis, which is orthogonal to  $S^2$  and is invariant under random rotations.

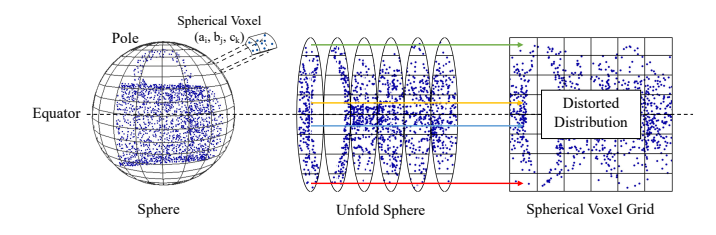


Fig. 3. Distorted distribution in spherical coordinates.

#### 4.2.1 Density Aware Factor.

 $\eta=\sin(\beta)$  is the density aware sampling factor. We treat spherical voxel signals as a tensor  $T\in\mathbb{R}^{I\times J\times K}$  with equalsized grids. However, these grids are not equal-sized in Euclidean space, making any point distributions distorted in spherical voxel grids, as shown in Figure 3.

*Proof.* Given the relationship from spherical coordinates (radius equals one) to Euclidean coordinates,

$$x = \sin(\beta)\cos(\alpha),$$
  

$$y = \sin(\beta)\sin(\alpha),$$
  

$$z = \cos(\beta).$$
 (5)

The Jacobian of differentials follows by:

$$\begin{bmatrix} \frac{\partial x}{\partial \alpha} & \frac{\partial x}{\partial \beta} & \frac{\partial x}{\partial r} \\ \frac{\partial y}{\partial \alpha} & \frac{\partial y}{\partial \beta} & \frac{\partial y}{\partial r} \\ \frac{\partial z}{\partial \alpha} & \frac{\partial z}{\partial \beta} & \frac{\partial z}{\partial r} \end{bmatrix}, \tag{6}$$

whose determinant equals  $sin(\beta)$ .

#### 4.3 Spherical Voxel Convolution

Given some spherical voxel signal  $f: S^2 \times H \to \mathbb{R}^{C_{in}}$ , we introduce Spherical Voxel Convolution (SVC) to further refine the features, while keeping it rotation invariant. This step implements the operator  $\Phi: \mathbb{R}^{S^2 \times H \times C_{in}} \to \mathbb{R}^{S^2 \times H \times C_{out}}$ .

Compared with Spherical CNN [4] where only spherical signals defined in  $S^2$  get convoluted. We propose the spherical voxel convolution which takes spherical signals defined in  $S^2 \times H$  as the input. To understand spherical voxel convolution, we first give some definitions and annotations. Here, we only consider functions with  $C_{in}=C_{out}=1$  to reduce clutter, while extensions to higher-dimension functions are straight-forward.

In order to define spherical voxel convolution, we need to first bridge  $S^2 \times H$  and SO(3) by several theorems and lemmas.

**Theorem 4.1** (Bijection from  $S^2 \times H$  to SO(3)). There exists a bijective map (almost everywhere)  $\mathcal{T}: S^2 \times H \to SO(3)$ , such that  $\mathcal{T}(s(\alpha,\beta),h) = R(\alpha,\beta,2\pi h) = Z(\alpha)Y(\beta)Z(2\pi h)$ .

*Proof.* This map is surjective because almost every element  $R \in SO(3)$  can be parameterized by ZYZ-Euler angles:  $(\alpha, \beta, \gamma)$ , and there is some  $x = (s(\alpha, \beta), \frac{\gamma}{2\pi})$  such that  $\mathcal{T}(x) = R(\alpha, \beta, \gamma)$ . To prove that this map in injective, suppose  $x_1 \neq x_2$ , by the bijective parameterization of  $S^2 \times H$ ,  $(\alpha_1, \beta_1, h_1) \neq (\alpha_2, \beta_2, h_2)$ , therefore  $\mathcal{T}(x_1) \neq \mathcal{T}(x_2)$  by the bijective parameterization of SO(3).

**Lemma 4.2.** For any  $x \in S^2 \times H$  and  $Q \in SO(3)$ , there exists some  $\theta$ , such that:

$$\mathcal{T}(Qx) = Q\mathcal{T}(x)Z(\theta),\tag{7}$$

where  $Z(\theta)$  is the rotation around z axes by  $\theta$ .

*Proof.* Writing left-hand side out and leverage Equation 1, we have:

$$\mathcal{T}(Qx(\alpha,\beta,h)) = \mathcal{T}(Qs(\alpha,\beta),h) \tag{8}$$

$$= \mathcal{T}(QZ(\alpha)Y(\beta)n, h), \tag{9}$$

Notice that  $QZ(\alpha)Y(\beta)$  is a general rotation and can be uniquely parameterized as  $Z(\alpha')Y(\beta')Z(\gamma')$ . Substitute this into Equation 9:

$$\mathcal{T}(Qx) = \mathcal{T}(Z(\alpha')Y(\beta')Z(\gamma')n, h) \tag{10}$$

$$= \mathcal{T}(Z(\alpha')Y(\beta')n, h) \tag{11}$$

$$= Z(\alpha')Y(\beta')Z(2\pi h) \tag{12}$$

$$= QZ(\alpha)Y(\beta)Z(-\gamma')Z(2\pi h) \tag{13}$$

$$= QZ(\alpha)Y(\beta)Z(2\pi h)Z(-\gamma') \tag{14}$$

$$= QT(x)Z(-\gamma'). \tag{15}$$

(11) follows from that rotations around z axes fix the north pole; (13) follows because  $QZ(\alpha)Y(\beta) = Z(\alpha')Y(\beta')Z(\gamma')$ ; (14) follows since rotations around z axes are commutative.  $\square$ 

**Definition 4.1** (Adjoint Function). The adjoint function  $f_{\mathcal{T}}: SO(3) \to \mathbb{R}$  of  $f: S^2 \times H \to \mathbb{R}$  with respect to  $\mathcal{T}$  is defined as:

$$f_{\mathcal{T}}(\mathcal{T}(x)) = f(x), x \in S^2 \times H.$$
 (16)

The adjoint function brings a function defined on  $S^2 \times H$  to SO(3).

Now, we are ready to give a formal definition of spherical voxel convolution, by leveraging SO(3) group convolution.

**Definition 4.2** (Spherical Voxel Convolution). Spherical voxel convolution, evaluated at point  $p \in S^2 \times H$  is defined as:

$$[\psi \star f](p) = \int_{\gamma} [\psi_{\mathcal{T}} \star f_{\mathcal{T}}](\mathcal{T}(p)Z(\gamma))d\gamma$$
$$= \int_{\gamma} \int_{SO(3)} \psi_{\mathcal{T}}(R^{-1}\mathcal{T}(p))f_{\mathcal{T}}(RZ(\gamma))dRd\gamma.$$
(17)

 $\psi, f: S^2 \times H \to \mathbb{R}$ , where f is input signal and  $\psi$  is the filter. Intuitively, our spherical voxel convolution is the corresponding adjoint SO(3) convolution averaged over the coset defined by  $Z(\gamma)$ .

**Definition 4.3** (Rotation Operator). We introduce a rotation function operator  $L_Q$ :

$$[L_Q f](x) = f(Q^{-1}x), Q \in SO(3).$$
 (18)

It follows that:

$$[L_Q f]_{\mathcal{T}}(x) = f_{\mathcal{T}}(\mathcal{T}(Q^{-1}x)) = f_{\mathcal{T}}(Q^{-1}\mathcal{T}(x)Z(\theta)).$$
 (19)

**Theorem 4.3** (Rotation Invariance). The spherical voxel convolution is point-wise rotation invariant when  $\psi_{\mathcal{T}}$  is constant on the right latitude:  $\psi_{\mathcal{T}}(R) \equiv \psi_{\mathcal{T}}(RZ(\theta))$ , for any  $R, \theta$ .

*Proof.* Suppose that the input point cloud is rotated by an arbitrary rotation Q, we have  $p \to Qp$ . As a consequence, the corresponding spherical signal is also rotated:  $f \to L_Q f$ , since f is sampled

П

from the original point cloud. We are now ready to prove the rotation invariance by applying SVC to the rotated input:

$$[\psi \star L_Q f](Qp)$$

$$= \int_{\gamma} \int_{SO(3)} \psi_{\mathcal{T}}(R^{-1} \mathcal{T}(Qp)) f_{\mathcal{T}}(Q^{-1} RZ(\theta + \gamma)) dR d\gamma$$
 (21)

$$= \int_{\gamma} \int_{SO(3)} \psi_{\mathcal{T}}(R^{-1}Q\mathcal{T}(p)) f_{\mathcal{T}}(Q^{-1}RZ(\theta + \gamma)) dR d\gamma \tag{22}$$

$$= \int_{SO(3)} \psi_{\mathcal{T}}(R^{-1}\mathcal{T}(p)) \int_{\gamma} f_{\mathcal{T}}(RZ(\theta + \gamma)) d\gamma dR$$
 (23)

$$= \int_{SO(3)} \psi_{\mathcal{T}}(R^{-1}\mathcal{T}(p)) \int_{\gamma} f_{\mathcal{T}}(RZ(\gamma)) d\gamma dR$$
 (24)

$$= \int_{\gamma} \int_{SO(3)} \psi_{\mathcal{T}}(R^{-1}\mathcal{T}(p)) f_{\mathcal{T}}(RZ(\gamma)) dR d\gamma$$
 (25)

$$= [\psi \star f](p). \tag{26}$$

(22) follows from Lemma 4.2 and  $\psi_{\mathcal{T}}(R) \equiv \psi_{\mathcal{T}}(RZ(\theta))$ ; (23) follows from the right invariance of SO(3) group integral [33]; (24) is a result of corollary (2.1) in [33].

It is obvious that SVC extracts the same feature no matter how the input point cloud rotates, which ensures point-wise **rotation invariance**.

In practice, Spherical Voxel Convolution (SVC) can be efficiently computed by Fast Fourier Transform (FFT) [34]. Convolutions are implemented by first doing FFT to convert both the input and filters into spectral domain, then multiplying them and converting results back to spatial domain, using Inverse Fast Fourier Transform (IFFT) [34].

#### 4.4 Point Re-sampling

After Spherical Voxel Convolution (SVC), we re-sample features at the location of original points, with *Trilinear Interpolation* as our operator  $\Lambda: \mathbb{R}^{S^2 \times H \times C} \to \mathbb{R}^{N \times C}$ . Each point's feature is a weighted average of nearest eight voxels, where the weights are inversely related to the distances to these spherical voxels. Then they are passed through fully connected layers to get the pointwise features.

#### 4.5 Architecture

To summarize, our rotation invariant function  $\mathcal F$  is a concatenation of the three modules/operators mentioned above:  $\mathcal Y=\Lambda(\Phi(\Gamma(\mathcal X)))$ . We first transform points from Euclidean space to unit spherical space by operator  $\Gamma$ , and then conduct a rotation invariant feature transform by operator  $\Phi$ , and finally re-sample the point features in Euclidean space by operator  $\Lambda$ .

After extracting point-wise rotation invariant features, we are able to do part segmentation by concatenating some fully connected layers. Our network could also realize object classification by placing a different head. In this case, we maxpool all the features in spherical voxels and pass this global feature through several fully connected layers, as shown in Figure 2.

# 5 SPRIN: Sparse Point-wise Rotation Invariant Network

In this section, we provide a sparse version of PRIN, which directly operates on the original sparse point cloud, making it more efficient and achieve the state-of-the-art performance.

# 5.1 Sparse Rotation Invariance

**Definition 5.1** (Point Cloud). A point cloud f can be expressed as:

$$f(x) = \sum_{i}^{N} \delta(x - x_i), \tag{27}$$

where  $\delta$  is the Dirac delta function,  $x_i$  are input points. This is different from that in Section 4.2, where we reconstruct the dense signal through an adaptive sampling method.

**Definition 5.2** (Sparse Correlation). In SPRIN, both input and output are the sparse points of original point cloud. We directly take  $S^2 \times H$  correlation between the filter and the point cloud, evaluated at some point  $x_i$ :

$$[\psi * f](x_j) = \int_{S^2 \times H} \psi(\mathcal{T}(x_j)^{-1} x) f(x) dx \tag{28}$$

$$= \sum_{i}^{N} \int_{S^2 \times H} \psi(\mathcal{T}(x_j)^{-1} x) \delta(x - x_i) dx \quad (29)$$

$$=\sum_{i}^{N}\psi(\mathcal{T}(x_{j})^{-1}x_{i})\tag{30}$$

**Theorem 5.1** (Sparse Point-wise Rotation Invariance). *The sparse correlation is point-wise rotation invariant when*  $\psi$  *is constant on the left coset of*  $Z(\theta)$ :  $\psi(x) \equiv \psi(Z(\theta)x)$ , *for any*  $x, \theta$ .

Proof.

$$[\psi * L_Q f](Qx_j) \tag{31}$$

$$= \int_{S^2 \times H} \psi(\mathcal{T}(Qx_j)^{-1}x) f(Q^{-1}x) dx$$
 (32)

$$= \int_{S^2 \times H} \psi(Z(-\theta)\mathcal{T}(x_j)^{-1}Q^{-1}x) f(Q^{-1}x) dx$$
 (33)

$$= \int_{\mathbb{C}^2 \times H} \psi(\mathcal{T}(x_j)^{-1} x) f(x) dx \tag{34}$$

$$= [\psi * f](x_j). \tag{35}$$

In practice, we sum  $\psi$  over k nearest neighbors of  $x_j$  to reduce memory footprint.  $\psi$  is implemented as fully connected layers, which is constant on the latitude. In order to gain more expressibility, besides  $\mathcal{T}(x_j)^{-1}x_i$ , we augment  $\psi$  with six rotation invariant features, which are sides and inner-angles of the triangle formed by  $x_i, x_j$  and  $\sum_i^N x_i$ .

# 5.2 Architecture

SPRIN architecture is shown in Figure 4. It progressively conducts sparse rotation invariant spherical correlation 5.2 between every point and its k nearest neighbors. The dilated kNN module is leveraged, which is similar to that of [18]. Given a center point  $x_j$  and a dilation rate d, output of the dilated kNN search is an index set of k/d points, which are randomly chosen from the nearest k neighbors. To hierarchical propagate low-level information to a larger high-level region, we leverage a similar operation set abstraction with PointNet++ [35]. Our set abstraction layer only contains a farthest point sampling module, which defines the evaluating point of following sparse spherical correlation layers.

For part segmentation, we incorporate two feature propagation layers are concatenated to up-sample the point cloud. This operation is similar to that in PointNet++ [35] while our model does

								A	rbitrary	Rotat	ion								No Ro	otation
	avg.	avg.	air	bag	cap	car	chair	ear	guitar	knife	lamp	laptop	motor	mug	pistol	rocket	skate	table	avg.	avg.
	inst.	cls.	plane	oug	Сир	Cui	Ciidii	phone	Surtai	Killic	шпр	партор	bike	mag	pistor	TOCKET	board	tuoic	inst.	cls.
PointNet [1]	31.30	29.38	19.90	46.25	43.27	20.81	27.04	15.63	34.72	34.64	42.10	36.40	19.25	49.88	33.30	22.07	25.71	29.74	83.15	78.95
PointNet++ [2]	36.66	35.00	21.90	51.70	40.06	23.13	43.03	9.65	38.51	40.91	45.56	41.75	18.18	53.42	42.19	28.51	38.92	36.57	84.63	81.52
RS-Net [23]	50.38	32.99	38.29	15.45	53.78	33.49	60.83	31.27	9.50	43.48	57.37	9.86	20.37	25.74	20.63	11.51	30.14	66.11	84.92	81.41
PCNN [17]	28.80	31.72	23.46	46.55	35.25	22.62	24.27	16.67	32.89	39.80	52.18	38.60	18.54	48.90	27.83	27.46	27.60	24.88	85.13	81.80
SPLATNet [24]	32.21	38.25	34.58	68.10	46.96	19.36	16.25	24.72	88.39	52.99	49.21	31.83	17.06	48.56	21.20	34.98	28.99	28.86	84.97	82.34
DGCNN [25]	43.79	30.87	24.84	51.29	36.69	20.33	30.07	27.86	38.00	45.50	42.29	34.84	20.51	48.74	26.25	26.88	26.95	28.85	85.15	82.33
SO-Net [27]	26.21	14.37	21.08	8.46	1.87	11.78	27.81	11.99	8.34	15.01	43.98	1.81	7.05	8.78	4.41	6.38	16.10	34.98	84.83	81.16
SpiderCNN [28]	31.81	35.46	22.28	53.07	54.2	22.57	28.86	23.17	35.85	42.72	44.09	55.44	19.23	48.93	28.65	25.61	31.36	31.32	85.33	82.40
SHOT+PointNet [9]	32.88	31.46	37.42	47.30	49.53	27.71	28.09	16.34	9.79	27.66	37.33	25.22	16.31	50.91	25.07	21.29	43.10	40.27	32.75	31.25
CGF+PointNet [10]	50.13	46.26	50.97	70.34	60.44	25.51	59.08	33.29	50.92	71.64	40.77	31.91	23.93	63.17	27.73	30.99	47.25	52.06	50.13	46.31
SRINet [16]	76.95	-	-	-	-	-	-	-	-	-	-	-	-	-	-	-	-	-	76.95	-
RIConv [19]*	-	75.30	80.60	80.00	70.80	68.80	86.80	70.30	87.30	84.70	77.80	80.60	57.40	91.20	71.50	52.30	66.50	78.40	-	-
Kim et al. [18]*	-	77.20	-	-	-	-	-	-	-	-	-	-	-	-	-	-	-	-	-	-
Ours(PRIN)	71.20	66.75	69.29	55.90	71.49	56.31	78.44	65.92	86.01	73.58	66.97	59.29	47.56	81.47	71.99	49.02	64.70	70.12	72.04	68.39
Ours(SPRIN)	81.92	78.34	81.36	79.18	77.10	74.17	87.71	73.01	90.16	83.04	79.58	85.82	68.88	92.45	77.27	51.11	73.48	79.06	81.88	78.21

#### TABLE 1

**Shape part segmentation results on ShapeNet part dataset.** Both average instance and average class IoUs (%) are reported. All models are trained on the non-rotated training set, then evaluated on the non-rotated and rotated test set, indicated by the labels. \*These results are reported trained with augmentation of rotations around *z* axes rather than no rotation: even under this unfair comparison, our method still outperforms them.

not induce any weight interpolation. It directly conducts sparse spherical correlation at those up-sampled points.

#### 6 EXPERIMENTS

In this section, we arrange comprehensive experiments to evaluate PRIN for point cloud analysis on different tasks. First, we demonstrate that our model can be applied to 3D shape part segmentation and classification with random rotations. Then, we provide some applications on 3D point matching and shape alignment. At last, we conduct ablation study to validate the design of each part.

# 6.1 Implementation Details.

PRIN and SPRIN are all implemented in Python using PyTorch on one NVIDIA GTX 1080 Ti. Adam optimization algorithm with learning rate 1e-2 is employed for PRIN, with a batch size of 8. RAdam [36] optimization algorithm with learning rate 1e-3 is employed for SPRIN, with a batch size of 12. The learning rate for PRIN decays with a rate of 0.5 every 5 epochs.

For PRIN, we set  $\xi=1/32$ . One spherical voxel convolution layer is utilized with channel 40. It is followed by two SO(3) group convolution layers with channel 40 and 50. All layers share the same bandwidth, which is 32. Two fully-connected layers with channels 50, 50 are concatenated for part segmentation.

For SPRIN, first two sparse spherical correlation layers are evaluated on all input points, with 2-strided 64-NN neighborhoods. Next three sparse spherical correlation layers are evaluated on 128 sampled points from the sampling & grouping module, with 3strided 72-NN, 1-strided 32-NN and 1-strided 32-NN neighborhoods, respectively. Then three sparse spherical correlation layers are evaluated on 32 sampled points from the sampling & grouping module, with 1-strided 32-NN neighborhoods. For classification, the max and avg pooling layer concatenates max-pooling and avgpooling results, followed by three fully-connected layers, with 256, 64, 40 channels respectively. For part segmentation, two sparse spherical correlation layers with 1-strided 16-NN and 1strided 32-NN are proposed at the first up-sampling level. Three sparse spherical correlation layers with 1-strided 32-NN, 2-strided 48-NN and 3-strided 96-NN are proposed at the second upsampling level. In the end, three fully connected layers with channels 128, 256, 50 are concatenated.

# 6.2 Part Segmentation on Rotated Shapes

#### 6.2.1 Dataset

ShapeNet part dataset [5] contains 16,881 shapes from 16 categories in which each shape is annotated with expert verified part labels from 50 different labels in total. Most shapes are composed of two to five parts. We follow the data split in PointNet [1]. 2048 points are sampled per shape for PRIN while 1024 points are sampled per shape for SPRIN because of memory limits.

# 6.2.2 Evaluation Results

Part segmentation is a challenging task for rotated shape analysis. We compare our method with various baseline methods and train each model on the non-rotated training set and evaluate them on the non-rotated and rotated test set. Qualitative results are shown in Figure 5. Both PRIN and SPRIN can accomplish part segmentation task on randomly rotated shapes without seeing these rotations. Even though state-of-the-art vanilla deep learning networks like PointNet++ [2], DGCNN [25] and SpiderCNN [28] can achieve fairly good results, they fail on the rotated point clouds. Besides, traditional local features based on local reference frames (LRF) like CGF [10] and SHOT [9] concatenated are also compared. For these descriptors, we train a PointNet-like network with CGF/SHOT features as the input. Although these descriptors are rotation invariant, their performance is inferior to ours. Pointlevel rotation invariant convolutions such as RIConv [19] and Kim et al. [18] are trained with z-axes rotation augmentation but still inferior to our SPRIN network.

Table 1 shows quantitative results of PRIN/SPRIN and baseline methods. We compare both mean instance IoU and mean class IoU for all the methods. Our SPRIN network even approaches the performance of modern deep learning methods when tested with no rotation. Figure 5 gives some visualization of results between state-of-the-art deep learning methods and PRIN/SPRIN over the ShapeNet part dataset. Biased by the canonical orientation of point clouds in the training set, networks like PointNet just learn a simple partition of Euclidean space, regardless of how the object is oriented. RIConv gives inaccurate segmentation results on part boundaries while our methods are able to give accurate results under arbitrary orientations.

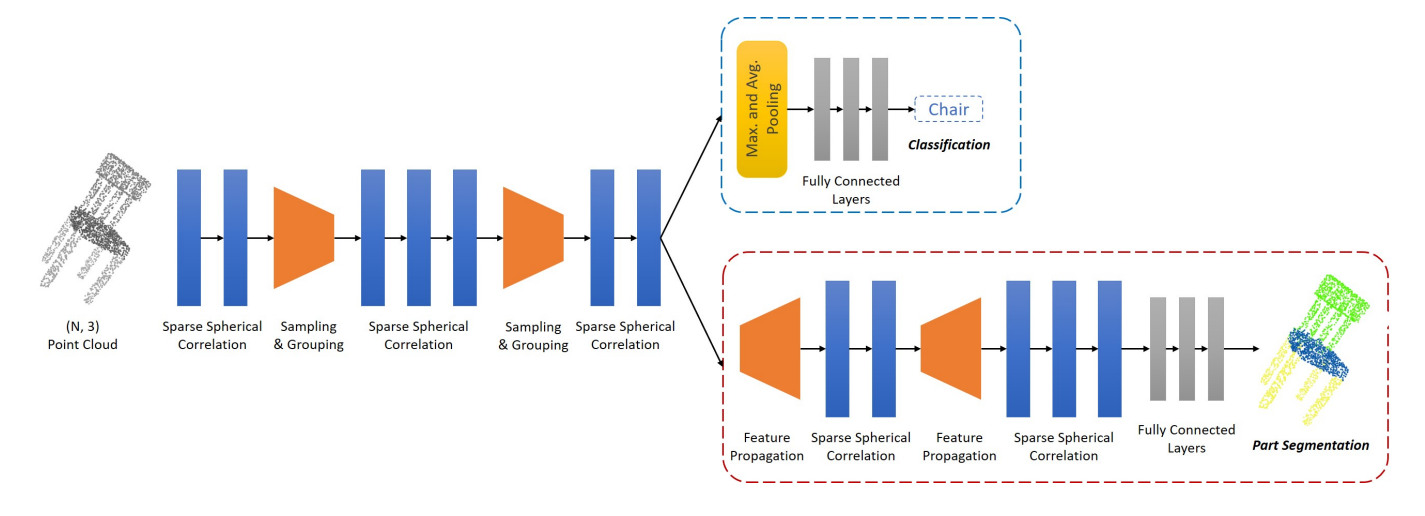


Fig. 4. **SPRIN Architecture.** SPRIN directly operates on sparse point clouds with several sparse spherical correlation layers. Farthest point sampling and kNN grouping are leveraged to aggregate information from low level to high level. Max and average pooling layers follows to extract global features and finally a classification score is given by fully-connected layers.

It should be also noticed that both PRIN and SPRIN have little performance drop when evaluated on the rotated test set, compared with that on the non-rotated set. This is also consistent with our theoretical analysis.

# 6.3 Classification on Rotated Shapes

#### 6.3.1 Dataset

ModelNet40 [6] is a 3D shape classification dataset which contains 12,308 shapes from 40 categories. Here, we use its corresponding point clouds dataset provided by PointNet [1]. 2048 points are sampled per shape for both PRIN and SPRIN.

Method	Input	NR	AR		
PointNet [1]		88.45	12.47		
PointNet++ [2]		89.82	21.35		
Point2Sequence [30]		92.60	10.53		
Kd-Network [31]		86.20	8.49		
Spherical CNN [3]		81.73	55.62		
DeepSets [29]	Point XYZ	88.73	9.72		
LDGCNN [26]	Point X 1 Z	92.91	17.82		
SO-Net [27]		93.44	9.64		
SRINet [16]		87.01	87.01		
RIConv [19]*		-	86.40		
Kim et al. [18]*		-	89.50		
Ours(PRIN)		79.76	72.43		
Ours(SPRIN)		85.19	85.40		
SHOT+PointNet [9]	Local Features	48.79	48.79		
CGF+PointNet [10]	Local realules	57.70	57.89		

#### TABLE 2

Classification results on ModelNet40 dataset. Performance is evaluated in average instance accuracy. NR means to train with no rotations and test with no rotations. AR means to train with no rotations and test with arbitrary rotations. \*These results are reported trained with augmentation of rotations around z axes, instead of no rotation: even under this unfair comparison, our method still gives competitive results.

#### 6.3.2 Evaluation Results

Though classification does not require point-wise rotation invariant features but a global feature, our network still benefits from DAAS and SVC.

We compare PRIN/SPRIN with several state-of-the-art deep learning methods that take point Euclidean coordinates and local rotation invariant features as the input. We train our network on the non-rotated training set and achieve 72.43% and 85.40% accuracy on the rotated test set, for PRIN and SPRIN respectively. Local rotation invariant features like CGF and SHOT are inferior to our method. The results are shown in Table 2. Almost all other deep learning methods fail to generalize to unseen orientations, except for Kim et al. [18], SRINet [16] and RIConv [19], compared with which, our methods still give competitive results.

#### 6.4 Application

**3D Rotation Invariant Point Descriptors.** For 3D objects, SHOT, CGF and other local features exploits local reference frames (LRF) as local descriptors. Similarly, PRIN/SPRIN is able to produce high quality rotation invariant 3D point descriptors, which is pretty useful as pairwise matching become possible regardless of rotations. In this application, we retrieve the closest descriptor from similar objects under arbitrary orientations. After that, point-level matching is conducted based on these rotation invariant point descriptors. A demonstration is shown in Figure 6. Through this matching process, we can find out where each point of the query object locates on another object. Moreover, such 3D point descriptors could have the potentiality to do scene searching and parsing as the degree of freedom reduces from six to three, leaving only translations.

To test the matching accuracy on ShapeNet part dataset, we compute and store point-wise features of 80% test objects (non-rotated) in ShapeNet as a database. Then we compute point-wise features of the other 20% test objects that are randomly rotated as queries. Feature retrievals are done by finding queries' nearest neighbours in the database. We evaluate against three different baselines to see if points corresponding to the same part are matched. The results are summarized in Table 3. Both PRIN and SPRIN outperform baseline methods by a large margin.

**Shape Alignment with Label Priors.** We now introduce a task that given some label prior in the Euclidean space, the goal is to align the point cloud to satisfy this requirement. For example, one may align a chair so that its back is on the top. So we add virtual

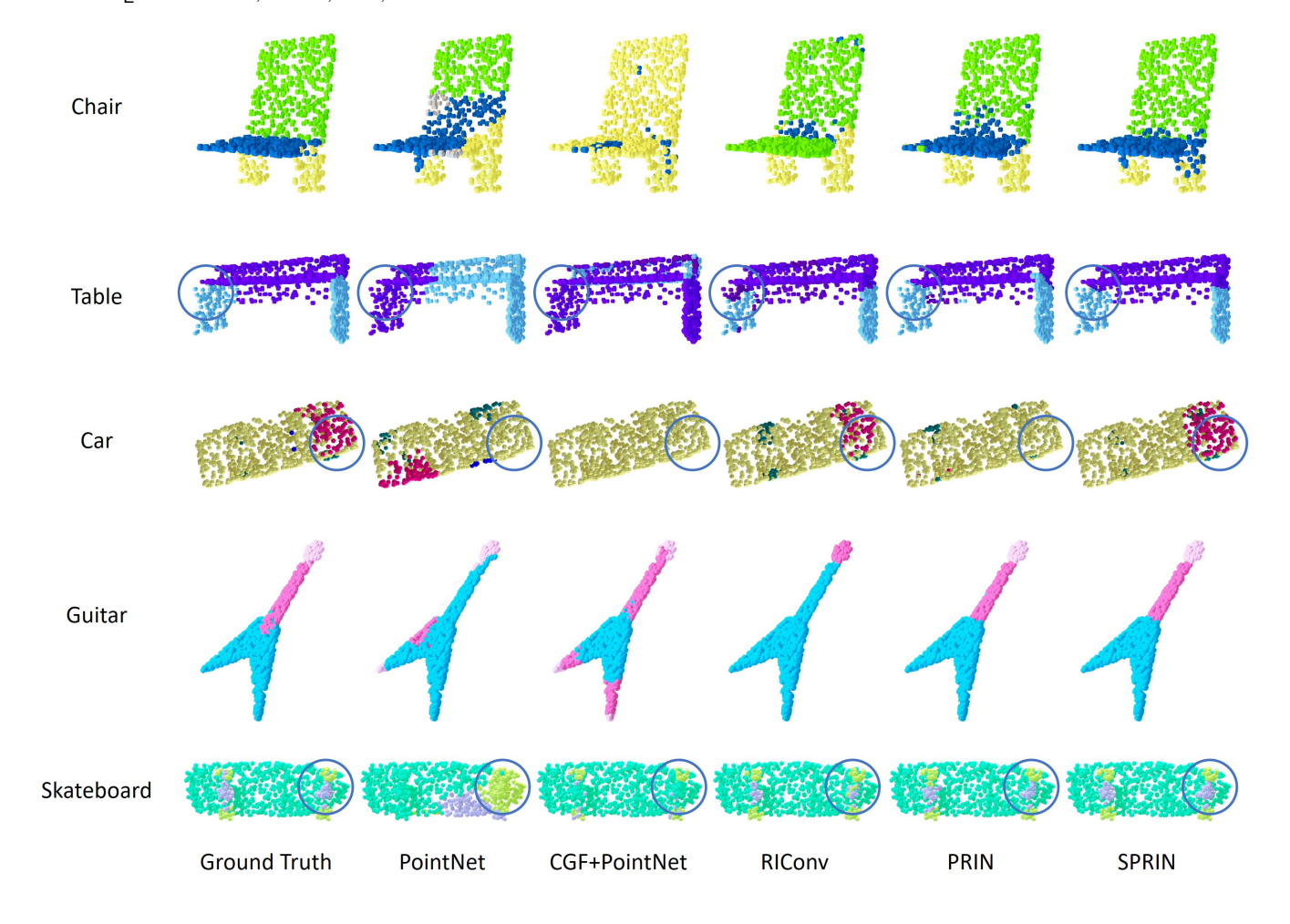


Fig. 5. **Visualization of results**. We compare the results of various methods on rotated point clouds, which are trained on the non-rotated dataset. Both PRIN and SPRIN generalize well to unseen orientations.

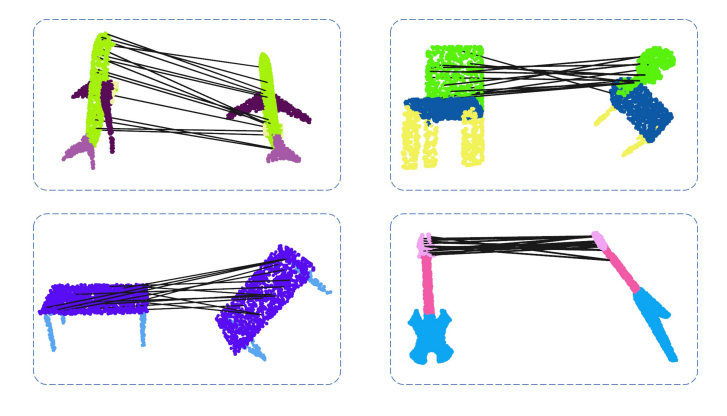


Fig. 6. **3D point matching results for PRIN.** Point matching results between the query object features (left) and the retrieved ones (right) under different orientations.

points describing the label requirement. Once the KL divergence between the predicted scores and the ground-truth labels of these virtual points is minimized, the chair is aligned with its back on the top. This is demonstrated in Figure 7.

Method	Matching Accuracy
PointNet [1]	38.91
SHOT [9]	17.11
CGF [10]	52.51
Ours(PRIN)	86.12
Ours(SPRIN)	78.92

TABLE 3

**3D descriptor matching results for various methods.** Accuracy is the number of matched points corresponding to the same part divided by the number of all matched points.

# 6.5 Ablation Study

In this section we evaluate numerous variations of our method to verify the rationality of network design. Experiment results are summarized in Table 4, 5 and Figure 8.

# 6.5.1 Network Bandwidth

One decisive factor of our network is the bandwidth. Bandwidth is used to describe the sphere precision, which is also the resolution on  $S^2 \times H$ . Mostly, large bandwidth offers more details of spherical voxels, such that our network can extract more specific point features of point clouds. While large bandwidth assures more specific representation of part knowledge, more memory cost is accompanied. Increasing bandwidth from 4 to 32 leads

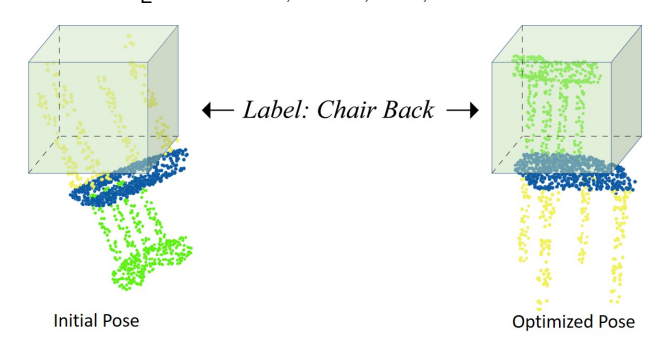


Fig. 7. Chair alignment with its back on the top. Left: A misalignment induces large KL divergence. **Right:** Required labels fulfilled with small KL divergence.

Bandwidth	DAAS	PRIN Acc./mIoU
32	Yes	85.99/71.20
16	Yes	84.84/68.09
8	Yes	82.58/65.43
4	Yes	72.20/52.98
32	No	83.13/67.47

#### TABLE 4

**Ablation study.** Test accuracy of PRIN on the rotated ShapeNet part dataset. Models with various bandwidths and sampling strategies are tested.

to a relative improvement of 16.04% and 25.59% on accuracy and mIoU, which is shown in Table 4.

# 6.5.2 Sampling Strategy

Recall that in Equation 3, we construct our signals on each spherical voxel with an density aware sampling filter. We now study the effect of Density Aware Adaptive Sampling (DAAS) and the results are given in Table 4. We see that using the  $sin(\beta)$  corrected sampling filter gives superior performance, which confirms our theory.

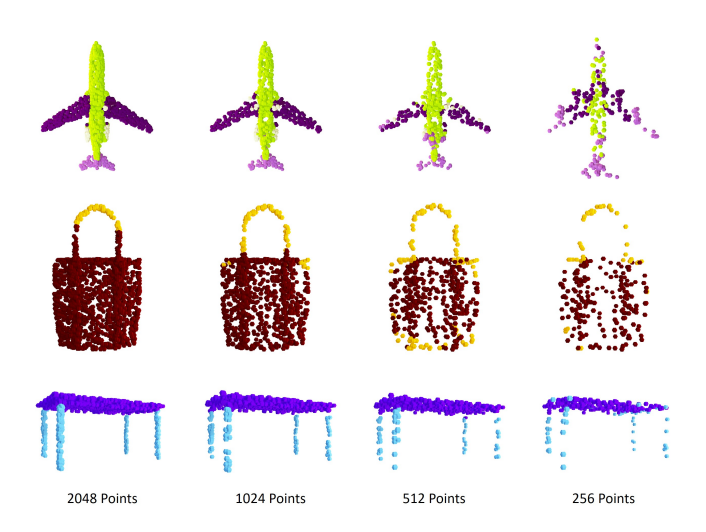


Fig. 8. Segmentation robustness visualization for PRIN. From left to right: we sample a subset of 2048, 1024, 512, 256 points from test point clouds respectively. We observe that our method is robust to missing points and gives consistent results.

# of points	PRIN Acc./mIoU	SPRIN Acc./mIoU
2048	85.99/71.20	-/-
1024	84.19/67.43	91.64/81.92
512	71.19/51.50	88.50/76.02
256	55.23/36.80	71.18/51.37

#### TABLE 5

**Qualitative results for segmentation robustness.** Test accuracy of PRIN/SPRIN on rotated ShapeNet part dataset. Various number of points are sub-sampled.

# 6.5.3 Segmentation Robustness

PRIN and SPRIN also demonstrate some robustness to corrupted and missing points. Although the density of point clouds declines, our network still segments correctly for each point. Qualitative results are given in Table 5. Both PRIN and SPRIN maintain a good accuracy up to 4x down-sampling. In Figure 8, we can see that PRIN predicts consistent labels regardless of the point density.

# 7 CONCLUSION

We present PRIN, a network that takes any input point cloud and leverages Density Aware Adaptive Sampling (DAAS) to construct signals on spherical voxels. Then Spherical Voxel Convolution (SVC) and Point Re-sampling follow to extract point-wise rotation invariant features. We place two different output heads to do both 3D point clouds classification and part segmentation. In addition, we extend PRIN to a sparse version called SPRIN, which directly operates on sparse point clouds. Our experiments show that both PRIN and SPRIN are robust to arbitrary orientations. Our network can be applied to 3D point feature matching and shape alignment with label priors. We show that our model can naturally handle arbitrary input orientations and provide detailed theoretical analysis to help understand our network.

# **ACKNOWLEDGMENTS**

This work is supported in part by the National Key R&D Program of China, No. 2017YFA0700800, SHEITC (2018-RGZN-02046) and Shanghai Qi Zhi Institute. This work was also supported by the National Natural Science Foundation of China under Grant 51675342, Grant 51975350 and Grants 61772332.

# REFERENCES

- [1] R. Q. Charles, H. Su, M. Kaichun, and L. J. Guibas, "Pointnet: Deep learning on point sets for 3d classification and segmentation," in 2017 IEEE Conference on Computer Vision and Pattern Recognition (CVPR), July 2017, pp. 77–85.
- [2] C. R. Qi, L. Yi, H. Su, and L. J. Guibas, "Pointnet++: Deep hierarchical feature learning on point sets in a metric space," in *Advances in neural* information processing systems, 2017, pp. 5099–5108.
- T. S. Cohen, M. Geiger, J. Köhler, and M. Welling, "Spherical cnns," International Conference on Learning Representations (ICLR), 2018.
- [4] C. Esteves, C. Allen-Blanchette, A. Makadia, and K. Daniilidis, "Learning so (3) equivariant representations with spherical cnns," in *Proceedings of the European Conference on Computer Vision (ECCV)*, 2018, pp. 52–68.
- [5] L. Yi, V. G. Kim, D. Ceylan, I.-C. Shen, M. Yan, H. Su, C. Lu, Q. Huang, A. Sheffer, and L. Guibas, "A scalable active framework for region annotation in 3d shape collections," SIGGRAPH Asia, 2016.
- [6] Z. Wu, S. Song, A. Khosla, F. Yu, L. Zhang, X. Tang, and J. Xiao, "3d shapenets: A deep representation for volumetric shapes," in *Proceedings of the IEEE conference on computer vision and pattern recognition*, 2015, pp. 1912–1920.

- [7] Y. You, Y. Lou, Q. Liu, Y.-W. Tai, L. Ma, C. Lu, and W. Wang, "Pointwise rotation-invariant network with adaptive sampling and 3d spherical voxel convolution," in *Proceedings of the AAAI Conference* on Artificial Intelligence, vol. 34, no. 07, 2020, pp. 12717–12724.
- [8] F. Stein and G. Medioni, "Structural indexing: Efficient 3-d object recognition," *IEEE Transactions on Pattern Analysis & Machine Intelligence*, no. 2, pp. 125–145, 1992.
- [9] F. Tombari, S. Salti, and L. Di Stefano, "Unique signatures of histograms for local surface description," in *Computer Vision – ECCV 2010*, K. Daniilidis, P. Maragos, and N. Paragios, Eds. Berlin, Heidelberg: Springer Berlin Heidelberg, 2010, pp. 356–369.
- [10] M. Khoury, Q.-Y. Zhou, and V. Koltun, "Learning compact geometric features," in *Proceedings of the IEEE International Conference on Computer Vision*, 2017, pp. 153–161.
- [11] S. Malassiotis and M. G. Strintzis, "Snapshots: A novel local surface descriptor and matching algorithm for robust 3d surface alignment," *IEEE Transactions on pattern analysis and machine intelligence*, vol. 29, no. 7, pp. 1285–1290, 2007.
- [12] Y. Guo, M. Bennamoun, F. Sohel, M. Lu, and J. Wan, "3d object recognition in cluttered scenes with local surface features: a survey," *IEEE Transactions on Pattern Analysis and Machine Intelligence*, vol. 36, no. 11, pp. 2270–2287, 2014.
- [13] R. Gens and P. M. Domingos, "Deep symmetry networks," in *Advances in neural information processing systems*, 2014, pp. 2537–2545.
- [14] T. S. Cohen and M. Welling, "Steerable cnns," arXiv preprint arXiv:1612.08498, 2016.
- [15] S. Dieleman, K. W. Willett, and J. Dambre, "Rotation-invariant convolutional neural networks for galaxy morphology prediction," *Monthly notices of the royal astronomical society*, vol. 450, no. 2, pp. 1441–1459, 2015.
- [16] X. Sun, Z. Lian, and J. Xiao, "Srinet: Learning strictly rotation-invariant representations for point cloud classification and segmentation," in *Pro*ceedings of the 27th ACM International Conference on Multimedia, 2019, pp. 980–988.
- [17] A. Poulenard, M.-J. Rakotosaona, Y. Ponty, and M. Ovsjanikov, "Effective rotation-invariant point cnn with spherical harmonics kernels," in 2019 International Conference on 3D Vision (3DV). IEEE, 2019, pp. 47–56.
- [18] S. Kim, J. Park, and B. Han, "Rotation-invariant local-to-global representation learning for 3d point cloud," arXiv preprint arXiv:2010.03318, 2020.
- [19] Z. Zhang, B.-S. Hua, D. W. Rosen, and S.-K. Yeung, "Rotation invariant convolutions for 3d point clouds deep learning," in 2019 International Conference on 3D Vision (3DV). IEEE, 2019, pp. 204–213.
- [20] X. Li, R. Li, G. Chen, C.-W. Fu, D. Cohen-Or, and P.-A. Heng, "A rotation-invariant framework for deep point cloud analysis," arXiv preprint arXiv:2003.07238, 2020.
- [21] D. Maturana and S. Scherer, "Voxnet: A 3d convolutional neural network for real-time object recognition," in 2015 IEEE/RSJ International Conference on Intelligent Robots and Systems (IROS), Sept 2015, pp. 972–978
- [22] H. Su, S. Maji, E. Kalogerakis, and E. Learned-Miller, "Multi-view convolutional neural networks for 3d shape recognition," in *Proceedings* of the IEEE international conference on computer vision, 2015, pp. 945– 953.
- [23] Q. Huang, W. Wang, and U. Neumann, "Recurrent slice networks for 3d segmentation of point clouds," in *Proceedings of the IEEE Conference* on Computer Vision and Pattern Recognition, 2018, pp. 2626–2635.
- [24] H. Su, V. Jampani, D. Sun, S. Maji, E. Kalogerakis, M.-H. Yang, and J. Kautz, "SPLATNet: Sparse lattice networks for point cloud processing," in *Proceedings of the IEEE Conference on Computer Vision and Pattern Recognition*, 2018, pp. 2530–2539.
- [25] Y. Wang, Y. Sun, Z. Liu, S. E. Sarma, M. M. Bronstein, and J. M. Solomon, "Dynamic graph cnn for learning on point clouds," ACM Transactions on Graphics (TOG), 2019.
- [26] K. Zhang, M. Hao, J. Wang, C. W. de Silva, and C. Fu, "Linked dynamic graph cnn: Learning on point cloud via linking hierarchical features," arXiv preprint arXiv:1904.10014, 2019.
- [27] J. Li, B. M. Chen, and G. Hee Lee, "So-net: Self-organizing network for point cloud analysis," in *Proceedings of the IEEE conference on* computer vision and pattern recognition, 2018, pp. 9397–9406.
- [28] Y. Xu, T. Fan, M. Xu, L. Zeng, and Y. Qiao, "Spidercnn: Deep learning on point sets with parameterized convolutional filters," in *Proceedings* of the European Conference on Computer Vision (ECCV), 2018, pp. 87– 102.

- [29] M. Zaheer, S. Kottur, S. Ravanbakhsh, B. Poczos, R. R. Salakhutdinov, and A. J. Smola, "Deep sets," in *Advances in neural information* processing systems, 2017, pp. 3391–3401.
- [30] X. Liu, Z. Han, Y.-S. Liu, and M. Zwicker, "Point2sequence: Learning the shape representation of 3d point clouds with an attention-based sequence to sequence network," in *Proceedings of the AAAI Conference* on Artificial Intelligence, vol. 33, 2019, pp. 8778–8785.
- [31] R. Klokov and V. Lempitsky, "Escape from cells: Deep kd-networks for the recognition of 3d point cloud models," in 2017 IEEE International Conference on Computer Vision (ICCV), Oct 2017, pp. 863–872.
- [32] P. J. Kostelec and D. N. Rockmore, "Soft: So (3) fourier transforms," Department of Mathematics, Dartmouth College, Hanover, NH, vol. 3755, 2007
- [33] "Harmonic analysis on so(3)," http://www2.math.ou.edu/~cremling/teaching/lecturenotes/ln-so3.pdf, accessed: 2021-02-09.
- [34] P. J. Kostelec and D. N. Rockmore, "Ffts on the rotation group," *Journal of Fourier analysis and applications*, vol. 14, no. 2, pp. 145–179, 2008.
- [35] C. R. Qi, L. Yi, H. Su, and L. J. Guibas, "Pointnet++: Deep hierarchical feature learning on point sets in a metric space," in Advances in Neural Information Processing Systems 30, 2017, pp. 5099–5108. [Online]. Available: http://papers.nips.cc/paper/ 7095-pointnet-deep-hierarchical-feature-learning-on-point-sets-in-a-metric-space. pdf
- [36] L. Liu, H. Jiang, P. He, W. Chen, X. Liu, J. Gao, and J. Han, "On the variance of the adaptive learning rate and beyond," arXiv preprint arXiv:1908.03265, 2019.